Melting of spatially modulated phases at domain wall/surface junctions in antiferrodistortive multiferroics

Anna N. Morozovska [1,2] Eugene A. Eliseev [3] Deyang Chen,[4] Vladislav Shvetz,[2]
Christopher T. Nelson,[5] and Sergei V. Kalinin[5,*]

[1]*Institute of Physics, National Academy of Sciences of Ukraine, 46, Prospekt Nauky, 03028 Kyiv, Ukraine*
[2]*Physics Faculty, Taras Shevchenko Kyiv National University, 01033 Kyiv, Ukraine*
[3]*Institute for Problems of Materials Science, National Academy of Sciences of Ukraine, Krjijanovskogo 3, 03142 Kyiv, Ukraine*
[4]*Institute for Advanced Materials and Guangdong Provincial Key Laboratory of Optical Information Materials and Technology,*
South China Academy of Optoelectronics, South China Normal University, Guangzhou 510006, China
[5]*Center for Nanophase Materials Sciences, Oak Ridge National Laboratory, Oak Ridge, Tennessee 37831, USA*

A physical understanding of the nature of spatially modulated phases (SMPs) in rare-earth-doped antiferrodistortive (AFD) multiferroics and how they behave close to surfaces and interfaces is lacking. Here the emergence of the antiferroelectric (AFE), ferroelectric (FE), or ferrielectric (AFE-FE) spatial modulation in the vicinity of the morphotropic phase transition in $La_xBi_{1-x}FeO_3$ ($x \sim 0.2$) is explored on the atomic level using high-resolution scanning transmission electron microscopy (HRSTEM). The suppression, or "melting," of the AFE-type SMP in the vicinity of the AFD twin wall/surface junction is revealed by HRSTEM in $La_{0.22}Bi_{0.78}FeO_3$ films and explained by the hybrid approach combining Landau-Ginzburg-Devonshire (LGD) phenomenology and the semimicroscopic four-sublattice model (FSM). The LGD-FSM approach reduces the problem of AFE (or AFE-FE) SMP emergence and stability to the thermodynamic analysis of the free-energy functional with AFE, FE, and AFD long-range order parameters and two master parameters: the FE-AFE coupling strength between four neighboring A sites and the nonstoichiometry factor, which are proportional to the variations of La concentration in $La_xBi_{1-x}FeO_3$ films. We establish that the surface-induced melting of SMPs and the associated broadening of AFE AFD domain walls minimize the film free energy under certain conditions imposed on the master parameters and gradient energy below the critical value. The observed behavior provides insight into the origin of SMPs in AFD multiferroics.

I. INTRODUCTION

Multiferroic materials with coupled ferroelectric (FE) or antiferroelectric (AFE), ferromagnetic or antiferromagnetic (AFM), and antiferrodistortive (AFD) long-range ordering remain at the forefront of modern materials science research. This interest is due both to the broad gamut of current and potential applications and to the continuous interest for fundamental physics studies [1–5]. In particular, applications such as ferroelectric tunneling barriers, light-assisted ferroic dynamics, spin-driven effects, and ultrafast magnetoelectric switching for memory applications are now at the forefront of research [6–8].

Among the material systems for these applications, particularly of interest are bulk and nanosized multiferroic $BiFeO_3$ (BFO) and its solid solutions [9–14]. Advances in applications necessitate a fundamental understanding of FE, AFE, and AFD order parameter dynamics in this material, which in turn necessitates the study of both mesoscale phenomena such as polarization switching and topological defects and atomic scale phenomena at surfaces and interfaces [15–18].

On the nanometer scale, the breakthrough in understanding the functional properties of ferroics and multiferroics has been achieved via scanning probe microscopy studies such as piezoresponse force microscopy [19,20] and scanning transmission electron microscopy (STEM) [21–24]. For BFO, these have been used to reveal the complex nanoscale evolution of the domain structure in thin films [25–30], including vortices and vertices [31–34]. Domain walls in BFO were found to exhibit unusual electrophysical properties such as conduction and enhanced magnetotransport [20,21,32,35–37].

However, while for pure BFO these studies provide high-veracity insight into polarization dynamics and domain structures, the situation becomes more complex for the rare-earth (RE) -doped BFO. In this case, in addition to the pure-phase AFD-FE ordering and canted antiferromagnetic subsystem, additional symmetry lowering, spatial modulation, and order parameters can emerge [38–44]. The polar order parameters predominantly manifest in the A-site sublattice, allowing a four-sublattice model (FSM) to be developed for the analytical description of the corresponding A-cation displacements $\mathbf{U}$ in $La_xBi_{1-x}FeO_3$ (BFO:La) polymorphs [38]. However, the FSM itself cannot provide a link between additional order parameters: four atomic displacements $\mathbf{U}^{(i)}$ of La/Bi cations, intrinsic long-range FE polarization $\mathbf{P}$, an antipolar parameter

*Corresponding author: sergei2@ornl.gov

A, and the AFD oxygen octahedron tilt **Φ**. The interplay between **A**, **P**, and **Φ** rules the phenomena taking place at the domain walls, surfaces, and interfaces of orthoferrites, where the role of the long-range electrostatic and elastic fields conditioned by the spatial confinement can be very significant, if not crucial. Complementary to the FSM, the Landau-Ginzburg-Devonshire (LGD) approach allows a high-veracity description of polarization dynamics on multiple length scales [12,13,18], but the corresponding coupling terms cannot be determined from mesoscopic models and necessitate atomistic studies. However, a clear physical understanding of the origin of the spatially modulated phases (SMPs) in RE-doped multi-ferroics and how they behave close to surfaces and interfaces is still missing [38].

Here we study the nature of SMPs in the La-doped BiFeO₃ and explore their behavior in the vicinity of surfaces, domain walls, and domain wall/surface junctions. We develop the LGD theory combined with the FSM and establish the primary driving forces for SMP formation. The "melting" of the spatial modulation in the vicinity of the twin AFD domain wall junction with the electrically open film surface is observed and quantified using the FSM. The melting effect manifests itself as a suppression of the antipolar (AFE) and/or polar (FE) atomic displacements at the wall between two AFD domains, when the wall approaches the electrically open surface of the film, up to the complete disappearance of the displacements at the surface. The origin of SMP melting is explained using LGD-FSM formalism, with special attention to the role of long-range stray electric fields and related depolarization effects in the vicinity of the domain wall/surface junction.

II. STEM STUDIES OF SPATIALLY MODULATED PHASES OF REDOPED BFO

In the bulk rhombohedral $R3c$ phase, BFO is a multiferroic material with a large FE polarization, AFD oxygen octahedral rotations, antiferromagnetic order, and long-range ferromagnetic order coexisting up to room and elevated temperatures [45,46]. Bulk BFO exhibits AFD long-range order at temperatures below 1200 K; it is FE with a large spontaneous polarization below 1100 K and is AFM below the Néel temperature $T_N \approx 650$ K [47]. Similar to other antiferrodistortive ferroelectrics, the behavior of the AFD order parameter at the domain walls of BFO determines their structure and energy [48].

On doping with La and other RE elements, BFO undergoes a transition from the rhombohedral (R) to the nonrhombohedral [e.g., orthorhombic (O)] AFE phase. Correspondingly, on the phase diagram these symmetry-incompatible phases are joined by the morphotropic phase boundaries. The La-doping concentration of 22% used in this work lies near the morphotropic phase boundary (MPB), exhibiting coexisting ferroelectric R and antiferroelectric O phases at room temperature. These phases exhibit distinctive large polar distortions of the La/Bi A site from pseudocubic positions. In the FE R phase, displacements are cooperative along the ⟨111⟩ polarization axis. In the antiferroelectric O phase, modulated displacements occur on alternating pairs of [101]pseudocubic planes [44]. The two phases are readily distinguished by this A-site behavior, this sublattice exhibiting a very high signal-to-noise
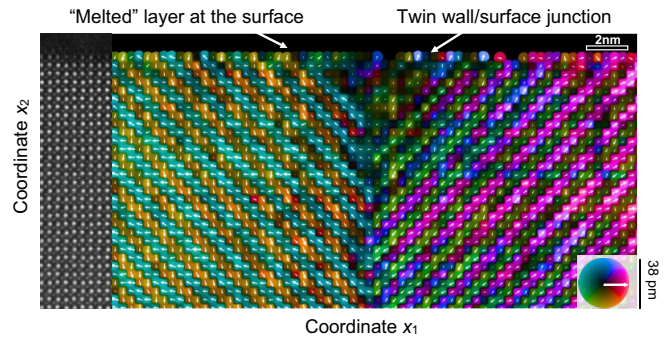

FIG. 1. Colorized map of A-site cations displacements from atomic-resolution HAADF STEM. The displacements are counted from their centrosymmetric positions. The two striped regions represent 109° twin domains of SMPs. The twin boundary is sharp in the bulk of the BFO:La film and melts approaching the free surface.

ratio in high-angle annular dark-field (HAADF) STEM imaging due to the strong high-angle scattering from the large-Z cations.

Here La₀.₂₂Bi₀.₇₈FeO₃ thin films were fabricated on SrTiO₃ (STO) buffered Si substrates with SrRuO₃ as the bottom electrode using pulsed laser deposition. The La concentration of the films was experimentally measured to be 22% from Rutherford backscattering spectroscopy. A colorized atomic scale [001] A-site displacement map is shown in Fig. 1 derived from HAADF STEM. Displacements correspond to A-cite cation positions relative to their centrosymmetric positions as defined by the neighboring B-site cations. Striped regions represent two SMP regions, separated by a 109° twin wall. The near-surface atomic layers clearly exhibit a suppressed AFE-type spatial modulation, called a melted layer. The domain wall, which is relatively sharp in the depth of the film, broadens and also exhibits damped modulations approaching the surface. The effect is called domain wall melting. The observed melting of the SMP in the vicinity of the domain/wall surface junction will be explored later using a combined LGD-FSM approach.

III. LANDAU-GINZBURG-DEVONSHIRE FORMALISM COMBINED WITH THE FOUR-SUBLATTICE MODEL

A. LGD thermodynamic potential

Continuum medium approaches, such as LGD thermodynamic potential combined with electrostatic equations and elasticity theory, allows self-consistent determination of polarization, structural order, electric and elastic fields in bulk and nanosized multiferroics, their surface, interfaces, antiphase boundaries, and 180° and twin domain walls of arbitrary geometry. The LGD functional of multiferroic, e.g., BFO:La utilizes Landau-type power expansion, which includes FE, AFE, and AFD orders and the biquadratic couplings between the order parameters, and the LGD potential is [9,12,13,24]

$$G_{LGD} = \int_{-\infty}^{\infty} dx_3 \int_{-\infty}^{\infty} dx_1 \int_0^h (G_{Landau} + G_{el}$$
$$+ G_{grad} + G_{fl} + G_{els}) dx_2 + G_S. \qquad (1)$$

Here G_{LGD} contains separate contributions of FE and AFE polarization components P_i and A_i and components of the pseudovector determining the out-of-phase static rotations of the oxygen octahedrons Φ_i (see Appendix A in the Supplemental Material [49]). The Landau energy includes FE, AFE, and AFD energies and their coupling energy

$$G_{\text{Landau}} = G_P + G_A + G_\Phi + G_{PA} + G_{\Phi A} + G_{P\Phi} \quad (2a)$$

$$G_P = a_i(T)P_i^2 + a_{ij}P_i^2 P_j^2 + a_{ijk}P_i^2 P_j^2 P_k^2, \quad (2b)$$

$$G_A = c_i(T)A_i^2 + c_{ij}A_i^2 A_j^2 + c_{ijk}A_i^2 A_j^2 A_k^2, \quad (2c)$$

$$G_\Phi = b_i(T)\Phi_i^2 + b_{ij}\Phi_i^2 \Phi_j^2 + b_{ijk}\Phi_i^2 \Phi_j^2 \Phi_k^2. \quad (2d)$$

Here the Einstein summation convention is employed over repeated indices. The coefficients a_i, c_i, and b_i are temperature dependent, $a_i = a_T(T - T_C)$, $c_i = c_T(T - T_A)$, and $b_i = b_T T_{q\Phi}[\coth(T_{q\Phi}/T) - \coth(T_{q\Phi}/T_\Phi)]$, where T_C and T_A are the temperatures of the FE and AFE phases' absolute instability, respectively, T_Φ is the AFD transition temperature, and $T_{q\Phi}$ is the characteristic Barrett-type temperature related to some vibrational modes [50,51].

For the sake of simplicity, we assume that the temperatures T_C and T_A are dependent on the small variations δy of relative concentration RE impurity, $\delta y(\mathbf{r}) = y(\mathbf{r}) - y_0$ and $0 \leqslant |\delta y| \ll y_0 < 1$. Below we consider the linear dependence, $T_C = T_{C0}(1 - k_C \delta y)$, and $T_A = T_{A0}(1 + k_A \delta y)$, and all other coefficients in Eqs. (2c) and (2d) are regarded as concentration independent. Since the FE-AFE transition takes place with an increase in RE impurity at a fixed temperature (e.g., room) and all other conditions, the assumption leads to the equalities $T_{A0} = T_{C0} = T_0$, $k_C = k_A = k$, $a_{ij} = c_{ij}$, and $a_{ijk} = c_{ijk}$, which are valid at fixed temperatures, in complete agreement with Kittel-type models. The expressions

$$a_i = a_T[T - T_0(1 - k\delta y)] = -a_T(T_0 - T)\left[1 - \frac{T_0 k}{T_0 - T}\delta y\right]$$

and

$$c_i = a_T[T - T_0(1 + k\delta y)] = -a_T(T_0 - T)\left[1 + \frac{T_0 k}{T_0 - T}\delta y\right]$$

allow us to introduce the dimensionless temperature-dependent parameter ϵ and express the coefficients a_i and c_i through it as follows:

$$\epsilon(\delta y) = \frac{T_0 k}{T_0 - T}\delta y, \quad a_0 = a_T(T_0 - T),$$

$$a_i = a_0(1 - \epsilon), \quad c_i = a_0(1 + \epsilon). \quad (2e)$$

It is important that the parameter ϵ is linearly proportional to the variation of RE impurity concentration $\delta y = y(\mathbf{r}) - y_0$, where $0 \leqslant |\delta y| \ll y_0 < 1$. Thus $\epsilon(\delta y)$ can be considered as a nonstoichiometric function.

Biquadratic coupling energies have the form

$$G_{PA} + G_{\Phi A} + G_{P\Phi}$$
$$= t_{ijkl}P_i P_j A_k A_l + \zeta_{ijkl}\Phi_i \Phi_j(P_k P_l + A_k A_l). \quad (2f)$$

The biquadratic coupling between FE and AFE orders is described by the temperature-independent tensor t_{ijkl} and the coupling between the AFD, FE, and AFE orders is described

by the temperature-independent tensor ζ_{ijkl}. The FE phase can be thermodynamically stable at $0 \leqslant \delta y \leqslant \delta y_{\text{cr}}$ for the nonzero AFE-FE coupling term G_{PA}. At $G_{PA} = 0$, the MPB between FE (R) and AFE (O) phases corresponds to $\delta y = 0$ (e.g., $y_0 = 20\%$–25% of La). Below we consider that the strength of FE-AFE coupling t_{ijkl} is defined by the dimensionless scalar parameter χ,

$$t_{ijkl} = \chi t_{ijkl}^0. \quad (2g)$$

Since the FE-AFE coupling should depend on δy, the parameter equal to $[\delta y]$ reflects the effect of RE doping on the coupling strength between the neighboring A-site cations. Note that we included only the biquadratic coupling between FE, AFE, and AFD orders, since the lower-order coupling of P_i, A_i, Φ_i, and their gradients is forbidden due to the symmetry of the $m3m$ parent phase.

The electrostatic energy has the form

$$G_{\text{el}} = -P_i E_i - \frac{\varepsilon_0 \varepsilon_b}{2}E_i^2, \quad (2h)$$

where E_i are the components of the long-range electric field related to the electrostatic potential ϕ in a standard way $E_i = -\partial\phi/\partial x_i$. The potential ϕ can be determined from electrostatic equations in a self-consistent manner. Inside the ferroelectric film, the potential satisfies the Poisson equation $\varepsilon_0 \varepsilon_b \Delta\phi - \text{div}\mathbf{P} = 0$, where ε_0 is a universal dielectric constant and ε_b is the dielectric permittivity of background [52].

The gradient (G_{grad}) and flexoelectric (G_{fl}) energies [42,53–55] are

$$G_{\text{grad}} = g_{ijkl}\left(\frac{\partial P_i}{\partial x_k}\frac{\partial P_j}{\partial x_l} + \frac{\partial A_i}{\partial x_k}\frac{\partial A_j}{\partial x_l}\right) + v_{ijkl}\frac{\partial \Phi_i}{\partial x_k}\frac{\partial \Phi_j}{\partial x_l}, \quad (3a)$$

$$G_{\text{fl}} = \frac{F_{ijkl}}{2}\left(P_k\frac{\partial \sigma_{ij}}{\partial x_l} - \sigma_{ij}\frac{\partial P_k}{\partial x_l}\right). \quad (3b)$$

Here g_{ijkl} is the gradient tensor of FE and AFE long-range order parameters, v_{ijkl} is the gradient tensor of the AFD long-range order parameter, σ_{ij} is the elastic stress tensor, and F_{ijkl} are the components of the flexoelectric coupling constant. Note that we apply in the following only one half $F_{ijkl}\sigma_{ij}\frac{\partial P_k}{\partial x_l}$ of the full Lifshitz invariant (3b). Application of either the term $F_{ijkl}\sigma_{ij}\frac{\partial P_k}{\partial x_l}$ or the term $\frac{F_{ijkl}}{2}(P_k\frac{\partial \sigma_{ij}}{\partial x_l} - \sigma_{ij}\frac{\partial P_k}{\partial x_l})$ results in the same equations of state, but affects the boundary conditions [56,57]. The reason for using only the part of the Lifshitz invariant in Eq. (3b) is that implementation of the full form causes poor convergence of the numerical code. Using the truncated form of Eq. (3b) can be justified by the smallness of the flexoelectric coupling strength as compared to the polarization gradient term, i.e., for $F_{klmn}^2 < g_{ijkl}s_{ijmn}$ [58].

The elastic energy G_{els} has the form

$$G_{\text{els}} = -s_{ijkl}\sigma_{ij}\sigma_{kl} - Q_{ijkl}\sigma_{ij}(P_k P_l + A_k A_l) - R_{ijkl}\sigma_{ij}\Phi_k\Phi_l. \quad (4)$$

The values s_{ijkl} are the components of the elastic compliances tensor. The elastic stress tensor σ_{ij} is self-consistently determined from elasticity theory equations. The last two terms in Eq. (4) are electrostriction and rotostrictive contributions, with strengths proportional to the tensors Q_{ijkl} and R_{ijkl}, respectively.

TABLE I. Free-energy parameters of BFO:La. Here FP denotes the fitting parameter; for AFD parameters see, e.g., Ref. [24].

Parameter	Designation	Numerical values for BFO:La	Ref.
effective permittivity	$\varepsilon_{\text{eff}} = \Sigma_i \varepsilon_{bi} + \varepsilon_{\text{el}}$ (dimensionless)	7	FP
dielectric stiffness	$a_T (\times 10^5 \, \text{C}^{-2} \, \text{J m/K})$	9	[12]
Curie temperature for P	$T_{C0}(\text{K})$	1300	[12]
P expansion, fourth order	$a_{ij} (\times 10^8 \, \text{C}^{-4} \, \text{m}^5 \, \text{J})$	$a_{11} = -13.5, a_{12} = 5$	[12]
P expansion, sixth order	$a_{ijk} (\times 10^9 \, \text{C}^{-6} \, \text{m}^9 \, \text{J})$	$a_{111} = 11.2, a_{112} = -3, a_{123} = -6$	[12]
FE-AFE coupling	$t^0_{ijkl} (\times 10^7 \, \text{C}^{-4} \, \text{m}^5 \, \text{J})$	$t^0_{11} = 1, t^0_{12} = 0.1, t^0_{44} = 0, t_{ijkl} = t^0_{ijkl}, |\chi| < 5$	FP
electrostriction	$Q_{ij}(\text{C}^{-2} \, \text{m}^4)$	$Q_{11} = 0.054, Q_{12} = -0.015, Q_{44} = 0.02$	[13]
elastic stiffness	$c_{ij}(\times 10^{11} \, \text{Pa})$	$c_{11} = 3.02, c_{12} = 1.62, c_{44} = 0.68$	[66]
P and A gradient coefficients	$g^0_{ijkl}(\times 10^{-10} \, \text{C}^{-2} \, \text{m}^3 \, \text{J})$	$g^0_{11} = 8, g^0_{12} = -0.5, g^0_{44} = 5, g_{ijkl} = g g^0_{ijkl}$	FP
AFD-FE coupling	$\xi_{ij}(\times 10^{29} \, \text{C}^{-2} \, \text{m}^{-2} \, \text{J/K})$	$\xi_{11} = -0.5, \xi_{12} = 0.5, \xi_{44} = -2.6$	[12]
tilt expansion, second order	$b_T [\times 10^{26} \, \text{J/(m}^5 \, \text{K})]$	4	[12]
rotostriction	$R_{ij}(\times 10^{18} \, \text{m}^{-2})$	$R_{11} = -1.32, R_{12} = -0.43, R_{44} = 8.45$	[13]
flexoelectric coefficients	$F_{ij}(\times 10^{-11} \, \text{m}^3/\text{C})$	$F_{11} = 2, F_{12} = 1, F_{44} = 0.5$	FP
surface energy coefficients	$a^{(S)}_i, c^{(S)}_i \, (\times \text{C}^{-2} \text{J m}^2)$	$c^{(S)}_i \to \infty, a^{(S)}_i = 0$	FP

The simplest form of the film surface energy G_S is

$$G_S = \int_{-\infty}^{\infty} dx_3 \int_{-\infty}^{\infty} \left(\frac{a^{(S)}_i}{2} P_i^2 + \frac{c^{(S)}_i}{2} A_i^2 + \frac{b^{(S)}_i}{2} \Phi_i^2 \right) dx_1. \quad (5)$$

The non-negative values $a^{(S)}_i$, $c^{(S)}_i$, and $b^{(S)}_i$ are surface energy coefficients, the values of which affect the order parameter behavior near the surface of the film. Looking at the experimental image shown in Fig. 1, hereinafter we consider the special case $c^{(S)}_i \to \infty$ corresponding to $A_i = 0$ at the surface and the condition $a^{(S)}_i = 0$ corresponding to $\partial P_i/\partial n = 0$. The conditions $A_i = 0$ and $\partial P_i/\partial n = 0$ correspond to the minimal broadening of FE-AFD walls near the surface and the maximal broadening of AFE-AFD and AFE-FE-AFD walls, which virtually agrees with the physical picture of the antipolar displacement suppression at the surface and along the wall (as shown in Fig. 1).

The free-energy parameters of BFO:La are listed in Table I. Note that the long-range FE, AFE, and AFD order parameters, introduced above, correspond to the distortions of the initial parent phase with cubic $m3m$ symmetry, and therefore only those components which are nonzero in the $m3m$ phase are listed in the table using Voight notation.

B. Link to the FSM

Using Dzyaloshinsky substitution [59], we relate the polar **P** and three antipolar (**A**, **B**, and **Ã**) order parameters with the four atomic displacements $U^{(m)}_i$ of A-site cations as

$$P_i = \frac{q}{2} \left(U^{(1)}_i + U^{(2)}_i + U^{(3)}_i + U^{(4)}_i \right),$$

$$A_i = \frac{q}{2} \left(U^{(1)}_i - U^{(2)}_i - U^{(3)}_i + U^{(4)}_i \right), \quad (6a)$$

$$B_i = \frac{q}{2} \left(U^{(1)}_i - U^{(2)}_i + U^{(3)}_i - U^{(4)}_i \right),$$

$$\tilde{A}_i = \frac{q}{2} \left(U^{(1)}_i + U^{(2)}_i - U^{(3)}_i - U^{(4)}_i \right). \quad (6b)$$

Here $q \cong \frac{Q^*}{a^3}$ is a dimension factor proportional to the effective Born charge Q^* divided by the cubic unit cell volume a^3

corresponding to the $m3m$ parent phase. The superscript $m = 1, 2, 3, 4$ enumerates the FSM displacement vectors **U**, which correspond to one of the four sublattices in $Bi_{1-y}RE_yFeO_3$, and the subscript $i = 1, 2, 3$ enumerates components of the vectors $U^{(m)}_i$ in the mth sublattice. Displacements $U^{(m)}_i$, which correspond to atomic displacements from the centrosymmetric positions, are experimentally observable by, e.g., HRSTEM. An example is shown in Fig. 2(a), which is a close-up of Fig. 1.

Substitution of Eqs. (6) in the free energy (1) leads to the hybrid-type LGD-FSM free energy, whose explicit form is listed in Appendix A in [49] for several specific cases. Possible long-range ordered phases in the LGD-FSM approach and necessary conditions of their stability are listed in Table II. There is an FE AFD phase, PE-FE and AFE AFD phases, which are spatially homogeneous, and at least two AFE AFD phases and one ferrielectric AFE-FE AFD phase, which can be spatially modulated if the strength of the polarization gradient energy is less than the critical value $g_{\text{cr}}(\epsilon)$ [60]. The strength of the gradient coefficient g is introduced as $g_{ijkl} = g g^0_{ijkl}$, where $|g^0_{ijkl}| \leqslant 1$. The homogeneous phases with coordinate-independent long-range order parameters correspond to the first four rows of Table II. The SMP AFE and AFD-FE AFD phases with the x-modulated antipolar long-range order correspond to the two last rows in Table II. Since all these phases are AFD, we omit the abbreviation in the table for the sake of brevity.

The phase diagram calculated for bulk BFO:La, which contains the regions of the spatially homogeneous and modulated FE, AFE, and ferrielectric AFE-FE AFD phases, is shown in Fig. 2(b). The regions of stability of these phases depend on the dimensionless parameters $\epsilon(\delta y)$ and $\chi(\delta y)$, introduced in Eqs. (2e) and (2g), respectively. The nonstoichiometric factor $\epsilon(\delta y)$ and the FE-AFE coupling strength $\chi(\delta y)$, which depend on the variation of RE concentration, can control the mutual asymmetry of four sublattices. Corresponding directions of A-site cation displacements **U** are shown by arrows in the second column of Table II. The homogeneous FE AFD phase is stable at $\epsilon < 0$ and homogeneous AFE AFD phases are stable at $\epsilon > 0$, where both conditions $\chi > \chi_{\text{cr}}(\epsilon)$ and $g > g_{\text{cr}}(\epsilon)$ are
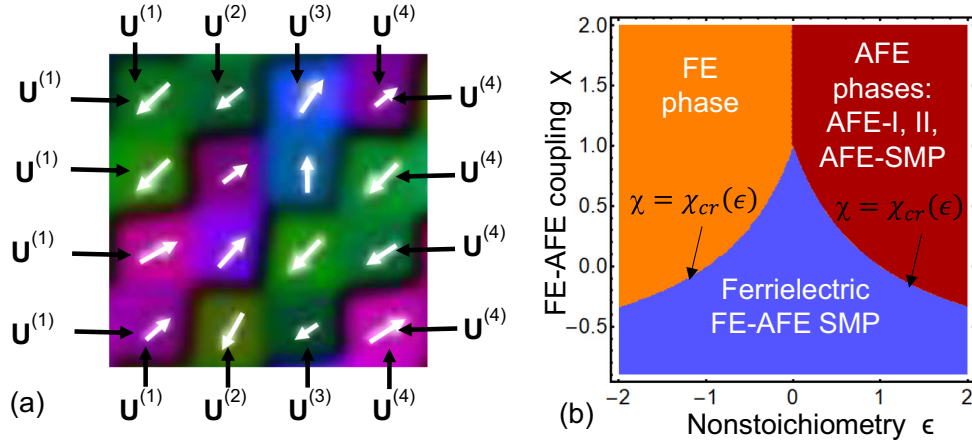
FIG. 2. (a) Part of colorized map of A-site polar displacements $\mathbf{U}^{(m)}$, which are experimentally observed from the HAADF STEM. White arrows show the value and direction of $\mathbf{U}^{(m)}$ for a sublattice with $m = 1, 2, 3, 4$. (b) Bulk phase diagram in dependence on the FE-AFE coupling strength χ and the nonstoichiometry factor ϵ. The structures of the FE, AFE, and ferrielectric FE-AFE AFD phases are listed in Table II (for more details see Appendix A in [49]).

necessary. A FE AFD phase corresponds to $P \neq 0$ and $A = 0$ and AFE AFD phases correspond to $A \neq 0$ and $P = 0$. The FE-AFE coexistence boundary $\epsilon = 0$ is almost independent of χ. The spatially modulated AFE phases can be stable at $\epsilon > 0$, $\chi > \chi_{\mathrm{cr}}(\epsilon)$, and $g < g_{\mathrm{cr}}(\epsilon)$. The spatially modulated ferrielectric AFE-FE phase can be stable for both signs of ϵ if $\chi < \chi_{\mathrm{cr}}(\epsilon)$ and $g < g_{\mathrm{cr}}(\epsilon)$.

To resume, the LGD-FSM approach reduces the description of the coexistence of different phases in the simplest case of the bulk BFO:La to the thermodynamic analysis of the free-energy functional with two dimensionless master parameters, the nonstoichiometric factor $\epsilon(\delta y)$ and the FE-AFE coupling strength $\chi(\delta y)$, both of which depend (e.g., are proportional) on the variations of RE concentration, and a strength g of the

gradient energy [which can be also δy dependent, but in a more complex way than $\epsilon(\delta y)$].

IV. FINITE-ELEMENT MODELING OF BFO: LA FILM WITH SMPS

To explain the observation of SMPs in thin La:BFO films and associated broadening of AFD domain walls at the wall/surface junction, shown in Fig. 1, we simulated the system properties using the LGD-FSM approach. The electrostatic and elastic part of the problem considers a BFO:La film of thickness h placed in perfect electric contact with a conducting bottom electrode that mechanically clamps the film at the surface $x_2 = 0$ (see Fig. 3). The top surface of the film ($x_2 = h$) is mechanically free and partially electrically

TABLE II. Long-range ordered AFD phases in the LGD-FSM approach and necessary conditions for their stability. Here PE denotes paraelectric.

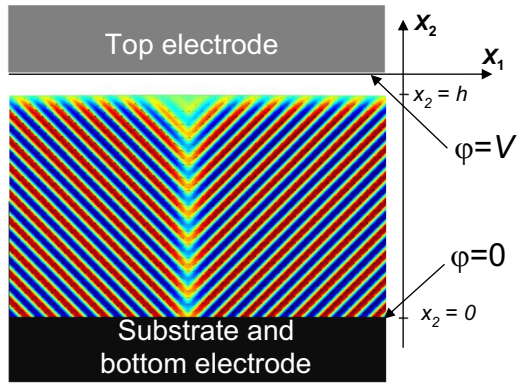|	Direction of displacements	Values of the order parameters	Necessary
Phase name	$U^{(1)}, U^{(2)}, U^{(3)},$ and $U^{(4)}$	$\boldsymbol{P}, \boldsymbol{A}, \boldsymbol{B},$ and $\tilde{\boldsymbol{A}}$	conditions
FE	↑↑↑↑	$\boldsymbol{P} = \boldsymbol{P}_S, \boldsymbol{A} = 0, \boldsymbol{B} = 0, \tilde{\boldsymbol{A}} = 0$	$\epsilon < 0,$
(R phase)	(all arrows have the same length)	$\boldsymbol{U}^{(1)} = \boldsymbol{U}^{(2)} = \boldsymbol{U}^{(3)} = \boldsymbol{U}^{(4)} = \boldsymbol{U}_S$	$\chi > \chi_{\mathrm{cr}}(\epsilon)$
AFE-I	↑↓↓↑ or ↓↑↑↓	$\boldsymbol{A} = \boldsymbol{A}_S$ (or $\tilde{\boldsymbol{A}} = \boldsymbol{A}_S$)	$\epsilon > 0,$
(O phase)	(all arrows have the same length)	$\boldsymbol{P} = 0, \boldsymbol{B} = 0, \tilde{\boldsymbol{A}} = 0$ (or $\boldsymbol{A} = 0$)	$\chi > \chi_{\mathrm{cr}}(\epsilon)$
		$\boldsymbol{U}^{(1)} = \boldsymbol{U}^{(2)} = -\boldsymbol{U}^{(3)} = -\boldsymbol{U}^{(4)} = \boldsymbol{U}_S$	
AFE-II	↑↓↑↓	$\boldsymbol{P} = 0, \boldsymbol{A} = 0, \tilde{\boldsymbol{A}} = 0, \boldsymbol{B} = \boldsymbol{B}_S,$	$\epsilon > 0,$
($O1$ phase)	(all arrows have the same length)	$\boldsymbol{U}^{(1)} = -\boldsymbol{U}^{(2)} = \boldsymbol{U}^{(3)} = -\boldsymbol{U}^{(4)} = \boldsymbol{U}_S$	$\chi < \chi_{\mathrm{cr}}(\epsilon)$
PE-AFE	↑ − ↓ − ↑ − ↓ −	$\boldsymbol{A} = \tilde{\boldsymbol{A}} = \boldsymbol{A}_S, \boldsymbol{P} = 0, \boldsymbol{B} = 0,$	$\chi < \chi_{\mathrm{cr}}(\epsilon)$
	(all arrows have the same length)	$\boldsymbol{U}^{(1)} = -\boldsymbol{U}^{(3)} = \boldsymbol{U}_S, \boldsymbol{U}^{(2)} = \boldsymbol{U}^{(4)} = 0$	
spatially modulated	↑↓↓↑↑↓↓↑ ↑↓↓↑↑↓↓↑↑↓↓↑	$\boldsymbol{A} = \boldsymbol{A}(x)$ [or $\tilde{\boldsymbol{A}} = \tilde{\boldsymbol{A}}(x)$]	$\epsilon > 0,$
AFE-I	(the arrows have different lengths modulated in space)	$\boldsymbol{P} = 0, \boldsymbol{B} = 0, \tilde{\boldsymbol{A}} = 0$ (or $\boldsymbol{A} = 0$)	$\chi > \chi_{\mathrm{cr}}(\epsilon),$
		$\boldsymbol{U}^{(1)} = \boldsymbol{U}^{(2)} = -\boldsymbol{U}^{(3)} = -\boldsymbol{U}^{(4)} = \boldsymbol{U}_A(x)$	$\mu < \mu_{\mathrm{cr}}(\epsilon)$
spatially modulated	↑↓↓↑↑↓↓↑ ↑↑↑↑↑↓↓↑↑↓↓↑	$\boldsymbol{P} = \boldsymbol{P}(x), \boldsymbol{A} = \boldsymbol{A}(x)$ [or $\tilde{\boldsymbol{A}} = \tilde{\boldsymbol{A}}(x)$],	
FE-AFE phase	(the arrows have different lengths modulated in space)	$\boldsymbol{B} = 0, \tilde{\boldsymbol{A}} = 0$ (or $\boldsymbol{A} = 0$),	$\chi < \chi_{\mathrm{cr}}(\epsilon),$
		$\boldsymbol{U}^{(1)} = \boldsymbol{U}^{(2)} = \boldsymbol{U}_P(x),$	$\mu < \mu_{\mathrm{cr}}(\epsilon)$
		$\boldsymbol{U} = \boldsymbol{U}^{(4)} = \boldsymbol{U}_A(x)$	

FIG. 3. Considered geometry of the BFO:La film with a melted spatial modulation of *A* site atomic displacements near the electrically open surface.

open, e.g., it can be separated from the top electrode by an ultrathin gap or covered with the surface screening charge, appearing due to surface states [61] or electrochemically active ions [62–65].

In the most common cases two combinations of atomic displacements out of four can be assumed to be zero, e.g., $\tilde{A}_i = B_i = 0$ (or $A_i = B_i = 0$). Corresponding displacements $U_i^{(m)}$ can be expressed via the nonzero polar parameter P_i and antipolar parameter A_i (or $\tilde{A}_i$) as $U_i^{(1)} = U_i^{(4)} = \frac{P_i + A_i}{2q}$ and $U_i^{(2)} = U_i^{(3)} = \frac{P_i - A_i}{2q}$. For any case $U_i^{(1)} = U_i^{(2)} = U_i^{(3)} = U_i^{(4)} = \frac{P_i}{2q}$ in the homogeneous FE AFD phase and $U_i^{(1)} = -U_i^{(2)} = -U_i^{(3)} = U_i^{(4)} = \frac{A_i}{2q}$ (or $U_i^{(1)} = U_i^{(2)} = -U_i^{(3)} = -U_i^{(4)} = \frac{\tilde{A}_i}{2q}$) in AFE AFD phases, which can be spatially modulated. All atomic displacements are nonzero in the AFE-FE AFD phase that is also spatially modulated. The case $\tilde{A}_i = B_i = 0$, considered hereinafter, allows us to make the elementary algebraic transformations listed in Appendixes A1 and A2 in [49] and to rewrite G_{LGD} in the form of Eqs. (A9) therein, which are used below. The case $A_i = B_i = 0$ can be considered in a very similar way.

Below, for the sake of simplicity, we limit our consideration to the cases when the AFD order parameter is almost constant and the dependence of Φ_i on coordinates can be neglected at room temperatures very far from the bismuth ferrite AFD transition temperature $T_\Phi = 1440$ K. Below we suppose that $\Phi_1 \approx \Phi_2 \approx \Phi_3 \approx \Phi_0$, where Φ_0 is the cooperative bulk value of the AFD order parameter, set equal to 23 pm at room temperature.

The system of coupled Euler-Lagrange equations was derived from the minimization of free energy [(A9) in [49]]. Allowing for Khalatnikov relaxation, the coupled equations for the AFE and FE long-range order parameters A_i and P_i acquire the form

$$\frac{\delta G_{LGD}}{\delta P_i} = -\Gamma_P \frac{\partial P_i}{\partial t}, \qquad \frac{\delta G_{LGD}}{\delta A_i} = -\Gamma_A \frac{\partial A_i}{\partial t}. \qquad (7a)$$

Here $i = 1, 2, 3$. The explicit form of Eqs. (7a) has the form of Eqs. (A10) and (A11) listed in Appendix A2 in [49]. Equations (7a) are supplemented by the following boundary

conditions at the film surfaces:

$$A_i|_{x_2=0,h} = 0, \qquad g_{ijkl} \frac{\partial P_j}{\partial x_k} n_l \bigg|_{x_2=0,h} = 0. \qquad (7b)$$

Note that we solve the dynamical problem (7) by finite-element modeling (FEM), being interested in equilibrium structures formed as a result of initial states relaxation. The exclusion of relaxation terms from the LGD-type equations (7a) greatly complicates the numerical calculations, since FEM for nonlinear equations necessarily requires either iterations or relaxation equations.

Elastic problem formulation is based on the modified Hooke's law obtained using the thermodynamic relation $u_{ij} = -\frac{\delta G_{els}}{\delta \sigma_{kl}}$, where u_{ij} are the components of the elastic strain tensor. Mechanical equilibrium conditions are $\partial \sigma_{ij}/\partial x_j = 0$. The film-substrate interface is strained, because the misfit strain close to -1% corresponds to the BFO/STO pair used in our experiments. Note that a misfit strain can greatly affect the film polar properties [66]. Material and fitting parameters used in FEM are listed in Table I.

The distributions of lateral components of AFE and FE order parameters, elastic strain, and electric potential are simulated near the junction of the $109°$ AFD twin wall with the surface of a BFO:La film. We superpose a random seeding at a regular $109°$ twin wall and study the system relaxation to an equilibrium state. The results of FEM are shown in Figs. 4 and 5 and Figs. A1 and A2 in [49], where we visualize the relaxed equilibrium distributions of **A** and **P** vectors, including their magnitude (colormap with a scale) and orientation (black arrows) in different phases.

The schemes of local *A*-cation displacement $\mathbf{U}^{(m)}$ distributions in four sublattices ($m = 1, 2, 3, 4$) for FE, ferrielectric AFE-FE, and two different AFE AFD phases are shown in Fig. 4(a). Note that the arrow lengths, which correspond to the absolute value of $\mathbf{U}^{(m)}$, can be different in the four neighboring sublattices in the AFE-FE and AFE-I AFD phases. The long-range modulation of the *U* length with a different period (e.g., from several to several tens of the four sublattices) corresponds to the SMP.

As anticipated from Fig. 2, the sign of the parameter ϵ switches the bulk of the film between the homogeneous FE and AFE phases and spatially modulated FE-AFE and AFE AFD phases. However, the situation in thin films, shown in Fig. 4, is more complex than in the bulk due to the presence of an electrically open surface $x_2 = h$.

Note that for the case $\epsilon < 0$, corresponding to the FE phase in a bulk, we found no AFE ordering even in the vicinity of the AFD twin wall, i.e., $\mathbf{A} = 0$ everywhere. The corresponding **P** distribution is shown in Fig. 4(b). The effect of domain wall broadening is insignificant, because the normal polarization gradient is absent at the surface, in accordance with the boundary condition (7b).

For the case $\epsilon > 0$, the gradual decrease of **P** and **A** vectors near the surface causes a significant broadening of the twin wall at the surface in the ferrielectric AFE-FE phase [see Figs. 4(c) and 4(d)] and in the pure AFE phase [Figs. 4(e) and 4(f)]. A slight asymmetry of the polarization distribution at the AFD twin wall junction with the surface can be seen in Figs. 4(d) and 4(f). The asymmetry is caused by the flexoelectric coupling. It is important that all the difference
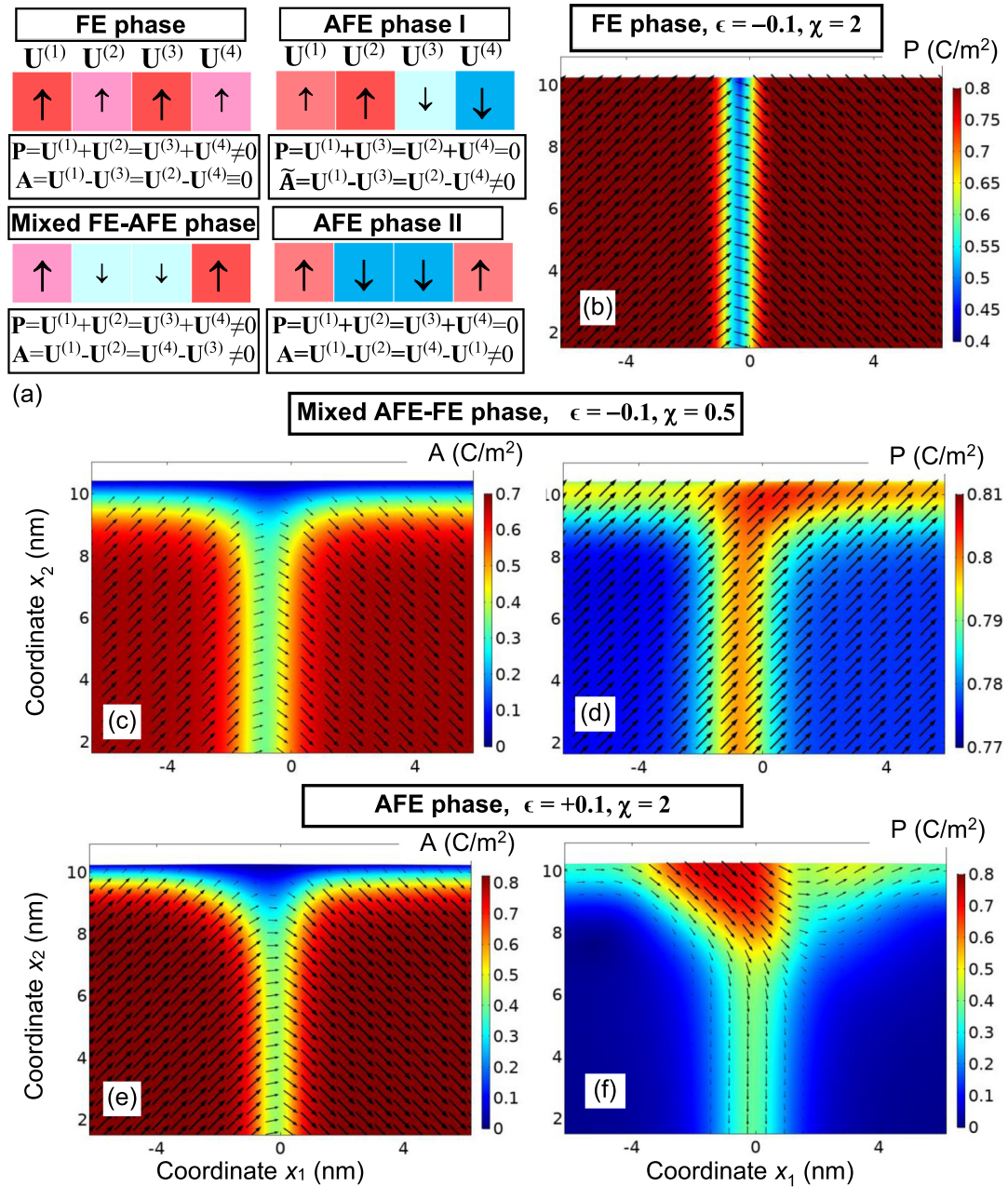
FIG. 4. (a) Schemes of local A-cation displacement $\mathbf{U}^{(m)}$ distributions in four sublattices ($m = 1, 2, 3, 4$) for FE, AFE, and AFE-FE AFD phases. Also shown are the distributions of (b), (d), and (f) the absolute value of the polarization vector $\mathbf{P}$ (in C/m^2) and (c) and (e) the antipolar order parameter $\mathbf{A}$ (in C/m^2) near the twin wall/surface junction in a 15-nm BFO film. Black arrows denote the local orientation and relative magnitude of the corresponding order parameter vector. The $\mathbf{P}$ and $\mathbf{A}$ distributions in three stable phases are shown: (b) the FE phase at $\chi = 2$ and $\epsilon = -0.1$, (c) and (d) the mixed AFE-FE phase at $\chi = 0.5$ and $\epsilon = -0.1$, and (e) and (f) the AFE phase at $\chi = 2$ and $\epsilon = 0.1$. The other parameters are listed in Table I. In addition, $T = 293$ K.

in parameters between the AFE-FE and AFE AFD phases are in the values of the AFE-FE coupling strength χ. Namely, a relatively small value $\chi = 0.5$ corresponds to the FE-AFE phase and a 4 times higher value $\chi = 2$ corresponds to the AFE phase, while the same positive values of ϵ and gradient coefficients g are used for Figs. 4(c)–4(f). This means that the primary driving mechanism for the AFE phase formation is the change of the AFE-FE coupling strength χ between four neighboring A-site cations caused by La doping.

Since the $\mathbf{A}$ vector vanishes when approaching the film surface due to the boundary condition $A_i = 0$ and decreases its value at the wall plane $x_1 = x_{\mathrm{DW}}$, the corresponding images in Figs. 4(c) and 4(e), where $\epsilon > 0$, apparently look like the melting effect of the AFD twin wall in the AFE-FE and AFE phases. At the same time, the $\mathbf{P}$ vector is nonzero at the wall and near the twin wall/surface junction and vanishing far from the wall region in the AFE phase, as shown in Fig. 4(f). This illustrates the fact that AFE order induces FE order at the AFD walls in BFO:La film due to the presence of biquadratic
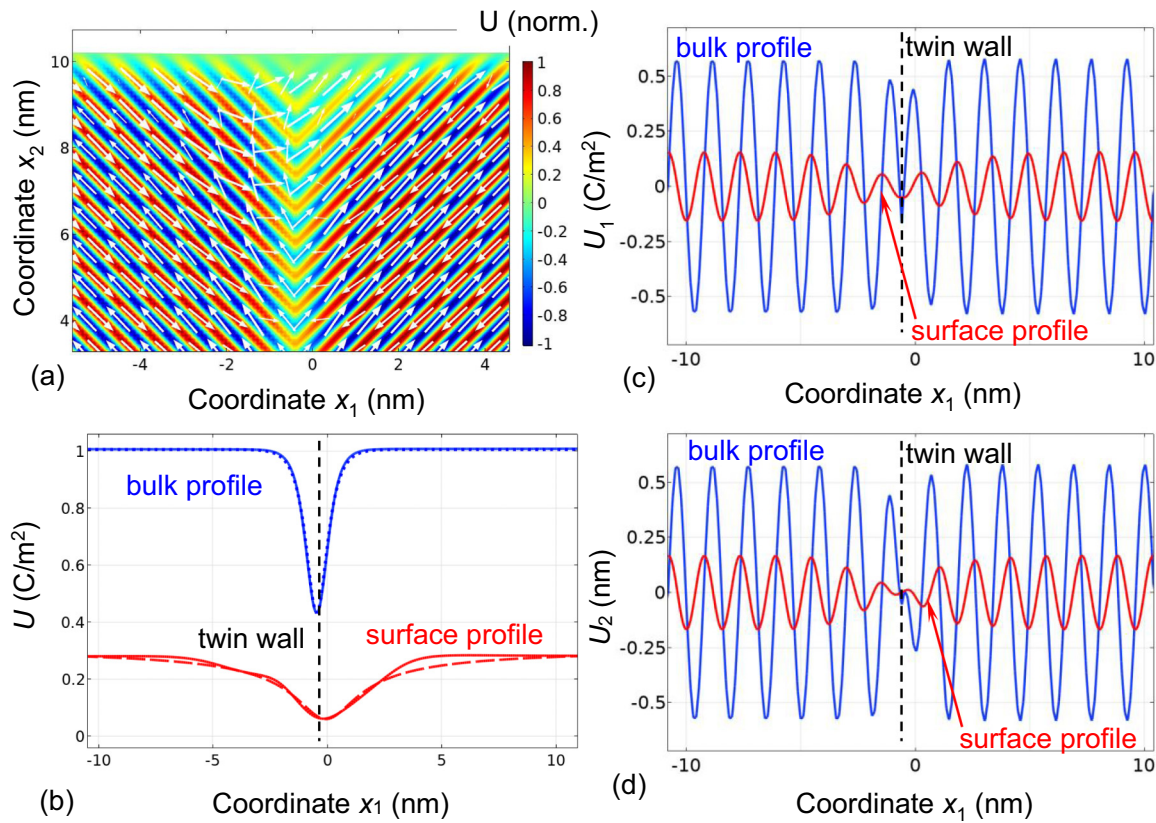
FIG. 5. (a) Color map of the *A*-site displacement value in the vicinity of AFE AFD twin wall/surface junction in a 15-nm BFO:La film. The white arrows show the direction and relative amplitudes of atomic displacements in different sublattices. (b) Profile of the displacement amplitude (i.e., envelope) *U* across the twin wall. Solid curves show FEM results; dotted and dashed curves are fit with Eqs. (8a) and (8b), respectively. The distributions of atomic displacements components (c) U_1 and (d) U_2 in the planes perpendicular to the domain wall, near and far from the film surface, are shown by blue curves and red curves, respectively. The other parameters are the same as in Figs. 4(e) and 4(f).

coupling between AFE and FE order parameters [see Eq. (2f)]. The effect of AFD wall broadening is significant for both vectors **P** and **A**.

Analysis of the FEM results allows us to conclude that the equilibrium distribution of **P** is determined by the optimal balance of the negative Landau energy G_{Landau}, which includes FE and AFE energies and FE-AFE coupling, the gradient energy G_{grad}, which is a positive quadratic form of **P** and **A** gradients, and the positive electrostatic energy G_{el} of the long-range depolarization electric fields induced by an abrupt polarization in the vicinity of electrically open film surface and elastic energy [see Eqs. (2)–(5) for details].

Since the AFE order parameter **A** cannot produce any sort of depolarization field, because $\varepsilon_0 \varepsilon_b \Delta \phi = \mathrm{div} \mathbf{P}$, the equilibrium distribution of **A** is primary determined by the optimal balance of the negative Landau energy G_{Landau}, positive gradient energy G_{grad}, and elastic energy G_{els}. The melting of the spatially modulated AFE phase in the vicinity of the AFD twin wall/surface junction is conditioned by the absence of the **A** contribution to the surface energy G_s (since $A_i = 0$ at the surface) and minimization of electrostatic energy near the film surface. Electrostriction and elastic energies G_{el} and G_{els}, respectively, induce additional anisotropy, but play a secondary role in the origin of the SMP melting effect. The energies G_{el} and G_{els} make a significant contribution to the correct

estimation of the domain wall width and decrease the wall broadening near the surface due to the self-clamping effect.

The colormap of *A*-site displacement in the vicinity of the AFE AFD twin wall/surface junction in a 15-nm BFO:La film is shown in Fig. 5(a). It can be seen that the displacement changes the sign in the neighboring sublattices (which corresponds to AFE order) but vanishes at the wall plane and near the surface. Note the apparent similarity of the color image with the experimental results shown in Fig. 1. The wall melting, shown in Fig. 5(a), manifests itself as a suppression of the AFE-type atomic displacements at the wall between two AFD domains, when the wall approaches the electrically open surface of the film, up to the complete disappearance of the displacements at the surface.

The smooth profile of the atomic displacement amplitude *U* (i.e., envelope) calculated across the AFD domain wall is shown in Fig. 5(b). Solid curves are FEM results, dotted and dashed curves are the interpolation functions, which are given by the expressions

$$U(x_1, x_2 \to \text{bulk}) = U_b - \frac{\delta U_b}{\cosh\left(\frac{x_1 - x_{\mathrm{DW}}}{L_b}\right)}, \qquad (8a)$$

$$U(x_1, x_2 = 0) = U_s - \frac{\delta U_s}{\sqrt{1 + (x_1 - x_{\mathrm{DW}})^2 / \xi_s^2}}. \qquad (8b)$$

The fitting parameters in Eqs. (8) are the bulk and surface amplitudes, $U_b = 1.00\,\mathrm{C/m^2}$, $\delta U_b = 0.57\,\mathrm{C/m^2}$, $U_s = 0.31\,\mathrm{C/m^2}$, $\delta U_s = 0.25\,\mathrm{C/m^2}$, analogs of correlation length $L_b = 0.415$ nm, $\xi_s = 1.3$ nm, and the domain wall position $x_{DW} = 0.2$ nm, which does not matter. The power-fading prefactor $\frac{\delta U_s}{\sqrt{1+(x_1-x_{DW})^2/\xi_s^2}}$ in Eq. (8b) indicates the existence of long-range stray electric fields, which cause the broadening of a AFE-FE AFD twin wall at the surface, supporting the tendency to minimize the system's electrostatic energy [67].

The melting of the SMP at the twin wall/surface junction is described quantitatively by Eqs. (8a) and (8b), since the difference of the atomic displacement amplitudes at the film surface, $U(x_{DW}, 0) = U_s - \delta U_s = 0.06\,\mathrm{C/m^2}$, appear small in comparison to the bulk value $U(x_{DW}, x_2 \to \mathrm{bulk}) = U_b - \delta U_b = 0.43\,\mathrm{C/m^2}$. It is seen from Eqs. (8a) and (8b) that the melting effect exists far from the wall also, while it is not as pronounced as at the surface, since the bulk displacement amplitude $U(|x_1| \gg x_{DW}, x_2 \to \mathrm{bulk})$ is more than several times higher than the amplitude at the surface $U(|x_1| \gg x_{DW}, 0)$, namely, $U_b > 3U_s$. The approximate dependence is valid

$$U(|x_1| \gg x_{DW},\ x_2) \cong U_b + (U_s - U_b)\exp\left(\frac{x_2}{\delta}\right), \quad (8c)$$

where $x_2 \leqslant 0$ and $\delta > 0$.

Distributions of atomic displacement components U_1 and U_2 in the planes perpendicular to the domain wall, near and far from the film surface, are shown in Figs. 5(c) and 5(d) by blue curves and red curves, respectively. In fact, the curves approximate the discrete atomic displacements in a continuous limit, namely, $U_i^{(m,n)} \to U_i(x_1, x_2)$ at fixed x_2. Following the simplest logic and using Eqs. (8a) and (8b), we obtain that the continuous limit $U_i(x_1, x_2)$ can be described by the interpolation functions

$$U_i(x_1, x_2 = 0)$$
$$= U(x_1, x_2 = 0)\sin\left(\frac{2\pi}{t_s}(x_1 - x_{DW}) + \psi_{si}\right), \quad (8d)$$

$$U_i(x_1, x_2 \to \mathrm{bulk})$$
$$= U(x_1, x_2 \to \mathrm{bulk})\sin\left(\frac{2\pi}{t_b}(x_1 - x_{DW}) + \psi_{bi}\right). \quad (8e)$$

Here $i = 1, 2$ denotes x_1 and x_2 components of the total vector $\mathbf{U}$ and the coordinate $x_2 \leqslant 0$. The amplitude $U(x_1, x_2 = 0)$ is given by Eq. (8b) and $U(x_1, x_2 \to \mathrm{bulk})$ is given by Eq. (8a). The periods t_S and t_b are very close to 1.6 nm, which corresponds to the quadrupling of the unit cell. To be consistent with Eqs. (8a) and (8b), the equality $U = \sqrt{U_1^2 + U_2^2}$ should be valid for Eqs. (8d) and (8e) and $U_2(x_{DW}, x_2) = 0$ at the AFD wall plane $x_1 = x_{DW}$. From these conditions the phases ψ_{si} and ψ_{bi} should equal to $\pm\frac{\pi}{2}$ for $i = 1$ and to $\pm\pi$ for $i = 2$. This is true for ψ_{si}; however, it appeared not so for

the phases ψ_{bi} of bulk profiles $U_i(x_1 = 0, x_2 \to \mathrm{bulk})$, shown by the blue curves in Figs. 5(c) and 5(d). The break of the phase ψ_{bi} at the wall plane and shift far from it are not related to the mesh discretization but rather illustrate the phase shift inherent to a long-range two- (or three-) dimensional SMP.

Hence, the developed hybrid-type LGD-FSM approach corroborates the statement that the driving forces of the order parameter spatial modulation and its melting in the vicinity of the AFD domain wall/surface junction in BFO:La film is primarily determined by the optimal balance of the order parameters' negative Landau energy and the positive energy of their gradients and long-range electric fields, $G_{\mathrm{Landau}} + G_{\mathrm{grad}} + G_{\mathrm{el}} = \min$. Electrostriction and elastic energies induce additional anisotropy and make a significant contribution to the domain wall width due to the self-clamping effect, but they play a secondary role in the origin of the SMP melting at the AFD wall. It is notable that the SMP arises as a result of coupling between the antipolar displacements $\mathbf{U}$ (inhomogeneous due to Bi/La substitution) reinforced by the total tilting Φ_0 of the oxygen octahedrons.

V. COMPARISON WITH EXPERIMENT

To reach a semiquantitative description of the Bi/La atomic displacement behavior and link it with Landau-type long-range polar and antipolar order parameters, we use the developed LGD-FSM approach. Experimental results for nonzero displacement components U_1 and U_2 are shown in Fig. 6. Symbols are HRSTEM experimental data; x_1 and x_2 scales are in nm and U_1 and U_2 are in pm.

It can be seen from Figs. 6(a) and 6(b) that the amplitude of AFE-type modulations decrease significantly when approaching the surface. This decrease quantitatively illustrates the effect of SMP melting, i.e., the reduction of the magnitude of the sign-alternating components U_1 and U_2 when approaching the surface and especially at the junction between the AFD domain wall and the surface. The decrease of the modulation depth on the left-hand sides of Figs. 6(a) and 6(b) is associated with the reduction of spatial modulation followed by the appearance of a homogeneous phase (see Fig. 1). The nonzero gradient of the envelope lines from Fig. 6 could be attributed to the presence of nonzero offset and linear drift related to the difficulties in separation of polar and nonpolar displacement of A cations. Note that the cross sections of Figs. 6(a) and 6(b) are chosen close to the domain wall plane, defined by the condition $x_1 = x_{DW}$, where $x_{DW} \approx 32$–33 nm.

To quantify the melting effect of polarization spatial modulation, the HRSTEM data are approximated by the oscillating function shown by solid curves in Fig. 6. The functions are periodically modulated with a spatially dependent phase and envelope:

$$U_i(x_1 = x_{DW} + \delta x, x_2) = R_{ai} + u_{ai}x_2 + \left[\alpha_i + \beta_i \exp\left(\frac{x_2}{\delta_i}\right)\right]\sin\left(\frac{2\pi x_2}{t_i} + \psi_{\alpha i}\right), \quad (9a)$$

$$U_i(x_1, x_2 \approx 0) = R_{bi} + u_{bi}x_1 + \left(\gamma_i - \frac{\delta\gamma_i}{\sqrt{1+(x_1-x_{DW})^2/\xi_i^2}}\right)\sin\left(\frac{2\pi}{t_i}(x_1 - x_{DW}) + \psi_{\gamma i}\right). \quad (9b)$$
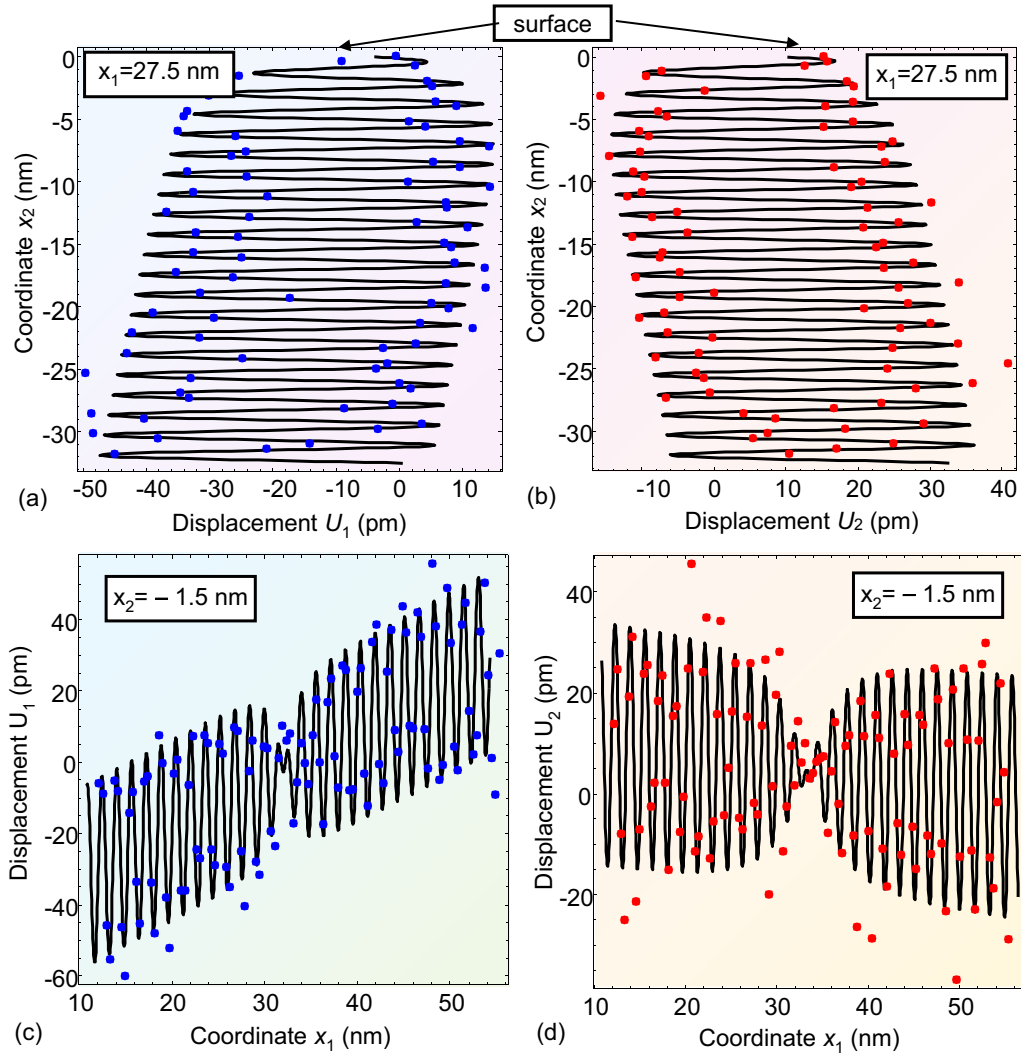
FIG. 6. Profiles of HAADF STEM atomic displacements corresponding to polar *A* cations (a) and (c) U_1 and (b) and (d) U_2 in different cross sections, namely, (a) and (b) in planes perpendicular to the film surface near the 109° twin domain wall with $x_1 = 27.5$ nm and (c) and (d) in subsurface planes parallel to the surface with $x_2 = -1.5$ nm. Symbols are experimental data; curves are calculated from Eqs. (9a) and (9b) with fitting parameters given in Tables III and IV.

Here $i = 1, 2$ denotes different components of the **U** vector and coordinate $x_2 \leqslant 0$. The value x_1 in Eq. (9a) is close to x_{DW} but not equal to it, e.g., we use $x_1 \approx 27$–28 nm. The fitting parameters R_{ai}, u_{ai}, α_i, β_i, $\psi_{\alpha i}$, R_{bi}, u_{bi}, γ_i, $\delta\gamma_i$, and $\psi_{\gamma i}$ are summarized in Tables III and IV.

The functional form (9) corresponds to the interpolation functions (8) derived to describe the FEM results shown in Fig. 5. Namely, in accordance with Eqs. (8c) and (8e), the third term in the function (9a) describes the exponential decay and oscillations in the x_2 direction of the displacement **U** calculated by FEM and shown in Figs. 5(a) and 5(b). The decay corresponds to $\alpha_i < 0$ and $\beta_i > 0$ (see Table III). The

third term in the function (9b) corresponds to the interpolation function (8d) describing the FEM results shown in Figs. 5(c) and 5(d) by red curves. The first two terms in Eqs. (9), $R_{ai} + u_{ai}x_2$ and $R_{bi} + u_{bi}x_1$, describe the base (offset and linear drift) of the raw HRSTEM data and are unrelated to the SMP behavior. The drift is absent for the theoretical curves shown in Figs. 5(c) and 5(d).

Equation (9a) fits the experimentally observed decay of the spatial modulation amplitude at $x_2 < 0$. The exponential decay describes quantitatively the melting effect in the x_2 direction. The power-fading prefactor $\frac{\delta\gamma_i}{\sqrt{1+(x_1-x_{\text{DW}})^2/\xi_i^2}}$ in Eq. (9b), which points to the existence of long-range electric fields,

TABLE III. Parameters for the x_1 cut of $U_i(x_1 = x_{\text{DW}} + \delta x, x_2)$ fitted by Eq. (9a).

N	R_{ai} (pm)	u_{ai}	α_i (pm)	$\psi_{\alpha i}/\pi$	δ_i (nm)	t_i (nm)	β_i (pm)	x_1 (nm)
$i = 1$	-7.24	4.32×10^{-2}	-26.3	0.228	2.41	1.61	22.7	27.5
$i = 2$	3.43	-3.70×10^{-2}	-21.2	0.240	2.41	1.61	21.5	27.5

TABLE IV. Parameters for the x_2 cut of $U_i(x_1, x_2 \approx 0)$ fitted by Eq. (9b).

N	R_{bi} (pm)	u_{bi}	γ_i (pm)	$\delta\gamma_i$ (pm)	$\psi_{\gamma i}/\pi$	ξ_i (nm)	t_i (nm)	x_{DW} (nm)
$i = 1$	−46.6	13.8×10^{-2}	21.3	15.2	−0.495	1.60	1.59	32.1
$i = 2$	12.4	-2.33×10^{-2}	20.5	14.3	−0.005	4.55	1.64	33.3

describes quantitatively the domain wall broadening at the surface. It can be seen from Tables III and IV that the decay length for surface effects $\delta_i = 2.4$ nm and the characteristic period of oscillations $t_i \approx 1.6$ nm are the same for both components and that the value 1.6 (nm) is approximately equal to four lattice constants (about 0.4 nm) at room temperature. This suggests that melted SMPs can be relatively well described by two-dimensional harmonic modulations $\sim \sin(\frac{2\pi x_2}{t_i} + \psi_{\alpha i})$ and $\sim \sin(\frac{2\pi x_1}{t_i} + \psi_{\gamma i})$ in Eqs. (9).

Hence the analysis of the experimental results with the fitting functions (9) allows us to conclude that the SMP melting at the AFE-AFD twin wall and the associated broadening of the wall near the surface are described, at least at the semiquantitative level, in the framework of the proposed hybrid-type LGD-FSM approach. Note that the hybrid-type LGD-FSM approach also allows us to reconstruct the behavior of polarization components, corresponding to the HRSTEM mapping shown in Fig. 1, using the expression for the polar displacement vector $\mathbf{P} = \frac{q}{2} \sum_{i=1}^{4} \mathbf{U}^{(i)}$ directly following from Eq. (6a).

VI. CONCLUSION

The emergence of the AFE or AFE-FE SMPs in the vicinity of morphotropic phase transition in the AFD multiferroic $La_xBi_{1-x}FeO_3$ ($x \sim 0.2$) was explored on the atomic level using HRSTEM imaging. Unexpectedly, the suppression, or melting, of the AFE-type spatial modulation was revealed near the AFD twin wall/surface junction in $La_{0.22}Bi_{0.78}FeO_3$ thin films.

The origin of the SMP melting was explained by the hybrid approach combining LGD phenomenology and the semimicroscopic FSM. The LGD-FSM approach reduced the problem of AFE (or AFE-FE) SMP emergence and phase transformations to the thermodynamic analysis of the free-energy functional with three long-range orders (polar FE, antipolar AFE, and AFD oxygen tilt) and two dimensionless master parameters: the FE-AFE coupling strength χ between four neighboring A sites and the nonstoichiometric factor ϵ, which are proportional to the variations δy of La concentration in $La_xBi_{1-x}FeO_3$ films. We calculated that the film phase diagram contains the FE, AFE, and AFE-FE AFD phases, whose stability is defined by the sign and values of ϵ and of χ and the gradient energy strength $g(\epsilon)$. The spatial modulation emerges in AFE and AFE-FE phases if the energy of the AFE and FE order parameters gradients is below the critical value.

We established that the surface-induced melting of the SMP and the associated broadening of the modulated AFE-AFD (or AFE-FE-AFD) domain walls originate from the system's tendency to minimize its free energy, consisting of the negative Landau energy of AFE and FE long-range order parameters, the positive energy of the order parameters

gradients, and the electrostatic energy excess induced by an abrupt electric polarization in the vicinity of electrically open film surface. The necessary conditions for the appearance of the melting effect are the certain conditions imposed on the master parameters ϵ and χ (listed in Table II) and gradient energy below the critical value $g < g_{cr}(\epsilon)$.

Hence, the formation of SMPs in the bulk and their melting in the vicinity of the surface and especially at the surface/domain wall junction were observed on the atomic level and quantified by the LGD-FSM approach. The observed behavior provides insight into the origin of SMPs in AFD multiferroics.

The Department of Energy will provide public access to the results of federally sponsored research in accordance with the DOE Public Access Plan [68].

[1] M. Fiebig, Revival of the magnetoelectric effect, J. Phys. D **38**, R123 (2005).

[2] N. A. Spaldin and M. Fiebig, The renaissance of magnetoelectric multiferroics, Science **309**, 391 (2005).

[3] A. P. Pyatakov and A. K. Zvezdin, Magnetoelectric and multiferroic media, Phys. Usp. **55**, 557 (2012).

[4] M. Fiebig, T. Lottermoser, D. Meier, and M. Trassin, The evolution of multiferroics, Nat. Rev. Mater. **1**, 16046 (2016).

[5] A. P. Pyatakov, Magnetoelectricity goes local: From bulk multiferroic crystals to ferroelectricity localized on magnetic topological textures, Physica B **542**, 59 (2018).

[6] P. Sharma, P. Schoenherr, and J. Seidel, Functional ferroic domain walls for nanoelectronics, Materials **12**, 2927 (2019).

[7] S. Kawachi, S. Miyahara, T. Ito, A. Miyake, N. Furukawa, J. Yamaura, and M. Tokunaga, Direct coupling of ferromagnetic moment and ferroelectric polarization in $BiFeO_3$, Phys. Rev. B **100**, 140412 (2019).

[8] C. Tzschaschel, T. Satoh, and M. Fiebig, Tracking the ultrafast motion of an antiferromagnetic order parameter, Nat. Commun. **10**, 3995 (2019).

[9] Y.-H. Chu, Q. Zhan, L. W. Martin, M. P. Cruz, P.-L. Yang, G. W. Pabst, F. Zavaliche, S.-Y. Yang, J.-X. Zhang, L.-Q. Chen, D. G. Schlom, I.-N. Lin, T.-B. Wu, and R. Ramesh, Nanoscale domain control in multiferroic $BiFeO_3$ thin films, Adv. Mater. **18**, 2307 (2006).

[10] Y.-H. Chu, L. W. Martin, M. B. Holcomb, M. Gajek, S.-J. Han, Q. He, N. Balke, C.-H. Yang, D. Lee, W. Hu, Q. Zhan, P.-L. Yang, A. Fraile-Rodríguez, A. Scholl, S. X. Wang, and R. Ramesh, Electric-field control of local ferromagnetism using a magnetoelectric multiferroic, Nat. Mater. **7**, 478 (2008).

[11] G. Catalan, J. Seidel, R. Ramesh, and J. F. Scott, Domain wall nanoelectronics, Rev. Mod. Phys. **84**, 119 (2012).

[12] D. V. Karpinsky, E. A. Eliseev, F. Xue, M. V. Silibin, A. Franz, M. D. Glinchuk, I. O. Troyanchuk, S. A. Gavrilov, V. Gopalan, L.-Q. Chen, and A. N. Morozovska, Thermodynamic potential and phase diagram for multiferroic bismuth ferrite ($BiFeO_3$), npj Comput. Mater. **3**, 20 (2017).

[13] A. N. Morozovska, E. A. Eliseev, M. D. Glinchuk, O. M. Fesenko, V. V. Shvartsman, V. Gopalan, M. V. Silibin, and D. V. Karpinsky, Rotomagnetic coupling in fine-grained multiferroic $BiFeO_3$: Theory and experiment, Phys. Rev. B **97**, 134115 (2018).

[14] J. Seidel, Nanoelectronics based on topological structures, Nat. Mater. **18**, 188 (2019).

[15] A. K. Yadav, C. T. Nelson, S. L. Hsu, Z. Hong, J. D. Clarkson, C. M. Schlepütz, A. R. Damodaran, P. Shafer, E. Arenholz, L. R. Dedon, D. Chen, A. Vishwanath, A. M. Minor, L. Q. Chen, J. F. Scott, L. W. Martin, and R. Ramesh, Observation of polar vortices in oxide superlattices, Nature (London) **530**, 198 (2016).

[16] E. Hassanpour, M. C. Weber, A. Bortis, Y. Tokunaga, Y. Taguchi, Y. Tokura, A. Cano, T. Lottermoser, and M. Fiebig, Interconversion of multiferroic domains and domain walls, arXiv:1908.06876.

[17] E. A. Eliseev, A. N. Morozovska, C. T. Nelson, and S. V. Kalinin, Intrinsic structural instabilities of domain walls driven by gradient couplings: meandering anferrodistortive-ferroelectric domain walls in $BiFeO_3$, Phys. Rev. B **99**, 014112 (2019).

[18] M. J. Han, E. A. Eliseev, A. N. Morozovska, Y. L. Zhu, Y. L. Tang, Y. J. Wang, X. W. Guo, and X. L. Ma, Mapping gradient-driven morphological phase transition at the conductive domain walls of strained multiferroic films, Phys. Rev. B **100**, 104109 (2019).

[19] C. Beekman, W. Siemons, M. Chi, N. Balke, J. Y. Howe, T. Z. Ward, P. Maksymovych, J. D. Budai, J. Z. Tischler, R. Xu, W. Liu, and H. M. Christen, Ferroelectric self-poling, switching, and monoclinic domain configuration in $BiFeO_3$ thin films, Adv. Funct. Mater. **26**, 5166 (2016).

[20] R. K. Vasudevan, W. Wu, J. R. Guest, A. P. Baddorf, A. N. Morozovska, E. A. Eliseev, N. Balke, V. Nagarajan, and P. Maksymovych, Domain wall conduction and polarization-mediated transport in ferroelectrics, Adv. Funct. Mater. **23**, 2592 (2013).

[21] J. Seidel, L. W. Martin, Q. He, Q. Zhan, Y.-H. Chu, A. Rother, M. E. Hawkridge, P. Maksymovych, P. Yu, M. Gajek, and N. Balke, Conduction at domain walls in oxide multiferroics, Nat. Mater. **8**, 229 (2009).

[22] J. A. Mundy, J. Schaab, Y. Kumagai, A. Cano, M. Stengel, I. P. Krug, D. M. Gottlob, H. Doğanay, M. E. Holtz, R. Held, and Z. Yan, Functional electronic inversion layers at ferroelectric domain walls, Nat. Mater. **16**, 622 (2017).

[23] W. Y. Wang, Y. L. Zhu, Y. L. Tang, M. J. Han, Y. J. Wang, and X. L. Ma, Atomic mapping of structural distortions in 109° domain patterned $BiFeO_3$ thin films, J. Mater. Res. **32**, 2423 (2017).

[24] M. J. Han, Y. J. Wang, D. S. Ma, Y. L. Zhu, Y. L. Tang, Y. Liu, N. B. Zhang, J. Y. Ma, and X. L. Ma, Coexistence of rhombohedral and orthorhombic phases in ultrathin $BiFeO_3$ films driven by interfacial oxygen octahedral coupling, Acta Mater. **145**, 220 (2018).

[25] J. Wang, J. B. Neaton, H. Zheng, V. Nagarajan, S. B. Ogale, B. Liu, D. Viehland, V. Vaithyanathan, D. G. Schlom, U. V. Waghmare, N. A. Spaldin, K. M. Rabe, M. Wuttig, and R. Ramesh, Epitaxial $BiFeO_3$ multiferroic thin film heterostructures, Science **299**, 1719 (2003).

[26] P. Maksymovych, M. Huijben, M. Pan, S. Jesse, N. Balke, Y.-H. Chu, H. J. Chang, A.Y. Borisevich, A. P. Baddorf, G. Rijnders, D. H. A. Blank, R. Ramesh, and S. V. Kalinin, Ultrathin limit and dead-layer effects in local polarization switching of $BiFeO_3$, Phys. Rev. B **85**, 014119 (2012).

[27] M. Trassin, G. De Luca, S. Manz, and M. Fiebig, Probing ferroelectric domain engineering in $BiFeO_3$ thin films by second harmonic generation, Adv. Mater. **27**, 4871 (2015).

[28] W. Y. Wang, Y. L. Tang, Y. L. Zhu, Y. B. Xu, Y. Liu, Y. J. Wang, S. Jagadeesh, and X. L. Ma, Atomic level 1D structural modulations at the negatively charged domain walls in $BiFeO_3$ films, Adv. Mater. Interf. **2**, 1500024 (2015).

[29] C. T. Nelson, P. Gao, J. R. Jokisaari, C. Heikes, C. Adamo, A. Melville, S.-H. Baek, C. M. Folkman, B. Winchester, Y. Gu, and Y. Liu, Domain dynamics during ferroelectric switching, Science **334**, 968 (2011).

[30] C. R. Winkler, A. R. Damodaran, J. Karthik, L. W. Martin, and M. L. Taheri, Direct observation of ferroelectric domain switching in varying electric field regimes using *in situ* TEM, Micron **43**, 1121 (2012).

[31] A. Gruverman, D. Wu, H.-J. Fan, I. Vrejoiu, M. Alexe, R. J. Harrison, and J. F. Scott, Vortex ferroelectric domains, J. Phys.: Condens. Matter **20**, 342201 (2008).

[32] N. Balke, B. Winchester, W. Ren, Y. H. Chu, A. N. Morozovska, E. A. Eliseev, M. Huijben, R. K. Vasudevan, P. Maksymovych, J. Britson, S. Jesse, I. Kornev, R. Ramesh, L. Bellaiche, L.-Q. Chen, and S. V. Kalinin, Enhanced electric conductivity at ferroelectric vortex cores in $BiFeO_3$, Nat. Phys. **8**, 81 (2012).

[33] B. Winchester, N. Balke, X. X. Cheng, A. N. Morozovska, S. Kalinin, and L. Q. Chen, Electroelastic fields in artificially created vortex cores in epitaxial $BiFeO_3$ thin films, Appl. Phys. Lett. **107**, 052903 (2015).

[34] W. Y. Wang, Y. L. Zhu, Y. L. Tang, Y. B. Xu, Y. Liu, S. Li, S. R. Zhang, Y. J. Wang, and X. L. Ma, Large scale arrays of four-state vortex domains in $BiFeO_3$ thin film, Appl. Phys. Lett. **109**, 202904 (2016).

[35] Q. He, C.-H. Yeh, J.-C. Yang, G. Singh-Bhalla, C.-W. Liang, P.-W. Chiu, G. Catalan, L. W. Martin, Y.-H. Chu, J. F. Scott, and R. Ramesh, Magnetotransport at Domain Walls in $BiFeO_3$, Phys. Rev. Lett. **108**, 067203 (2012).

[36] A. N. Morozovska, R. K. Vasudevan, P. Maksymovych, S. V. Kalinin, and E. A. Eliseev, Anisotropic conductivity of uncharged domain walls in $BiFeO_3$, Phys. Rev. B **86**, 085315 (2012).

[37] R. K. Vasudevan, A. N. Morozovska, E. A. Eliseev, J. Britson, J.-C. Yang, Y.-H. Chu, P. Maksymovych, L. Q. Chen, V. Nagarajan, and S. V. Kalinin, Domain wall geometry controls conduction in ferroelectrics, Nano Lett. **12**, 5524 (2012).

[38] S. Karimi, I. M. Reaney, Y. Han, J. Pokorny, and I. Sterianou, Crystal chemistry and domain structure of rare-earth doped $BiFeO_3$ ceramics, J. Mater. Sci. **44**, 5102 (2009).

[39] D. Kan, L. Pálová, V. Anbusathaiah, C. J. Cheng, S. Fujino, V. Nagarajan, K. M. Rabe, and I. Takeuchi, Universal behavior and electric field-induced structural transition in rare-earth substituted $BiFeO_3$, Adv. Funct. Mater. **20**, 1108 (2010).

[40] C.-J. Cheng, A. Y. Borisevich, D. Kan, I. Takeuchi, and V. Nagarajan, Nanoscale structural and chemical properties of antipolar clusters in Sm-doped $BiFeO_3$ ferroelectric epitaxial thin films, Chem. Mater. **22**, 2588 (2010).

[41] A. N. Morozovska, E. A. Eliseev, D. Chen, C. T. Nelson, and S. V. Kalinin, Building a free-energy functional from atomically resolved imaging: Atomic-scale phenomena in La-doped $BiFeO_3$, Phys. Rev. B **99**, 195440 (2019).

[42] A.Y. Borisevich, E. A. Eliseev, A. N. Morozovska, C.-J. Cheng, J.-Y. Lin, Y. H. Chu, D. Kan, I. Takeuchi, V. Nagarajan, and S. V. Kalinin, Atomic-scale evolution of modulated phases at the ferroelectric-antiferroelectric morphotropic phase boundary controlled by flexoelectric interaction, Nat. Commun. **3**, 775 (2012).

[43] R. Maran, S. Yasui, E. A. Eliseev, M. D. Glinchuk, A. N. Morozovska, H. Funakubo, I. Takeuchi, and N. Valanoor, Interface control of a morphotropic phase boundary in epitaxial samarium-modified bismuth ferrite superlattices, Phys. Rev. B **90**, 245131 (2014).

[44] D. Chen, C. T. Nelson, X. Zhu, C. R. Serrao, J. D. Clarkson, Z. Wang, Y. Gao, S.-L. Hsu, L. R. Dedon, Z. Chen, D. Yi, H.-J. Liu, D. Zeng, Y.-H. Chu, J. Liu, D. G. Schlom, and R. Ramesh, A strain-driven antiferroelectric-to-ferroelectric phase transition in La-doped $BiFeO_3$ thin films on Si, Nano Lett. **17**, 5823 (2017).

[45] D. C. Arnold, K. S. Knight, G. Catalan, S. A. T. Redfern, J. F. Scott, P. Lightfoot, and F. D. Morrison, The β-to-γ transition in $BiFeO_3$: A powder neutron diffraction study, Adv. Funct. Mater. **20**, 2116 (2010).

[46] R. Palai, R. S. Katiyar, H. Schmid, P. Tissot, S. J. Clark, J. Robertson, S. A. T. Redfern, G. A. Catalan, and J. F. Scott, β phase and γ-β metal-insulator transition in multiferroic $BiFeO_3$, Phys. Rev. B **77**, 014110 (2008).

[47] P. Fischer, M. Polomska, I. Sosnowska, and M. Szymanski, Temperature dependence of the crystal and magnetic structures of $BiFeO_3$, J. Phys. C **13**, 1931 (1980).

[48] O. Dieguez, P. Aguado-Puente, J. Junquera, and J. Iniguez, Domain walls in a perovskite oxide with two primary structural order parameters: First-principles study of $BiFeO_3$, Phys. Rev. B **87**, 024102 (2013).

[49] See Supplemental Material at http://link.aps.org/supplemental/10.1103/PhysRevB.102.075426 for calculation details.

[50] J. H. Barrett, Dielectric constant in perovskite type crystals, Phys. Rev. **86**, 118 (1952).

[51] Y. Gu, K. Rabe, E. Bousquet, V. Gopalan, and L.-Q. Chen, Phenomenological thermodynamic potential for $CaTiO_3$ single crystals, Phys. Rev. B **85**, 064117 (2012).

[52] A. K. Tagantsev and G. Gerra, Interface-induced phenomena in polarization response of ferroelectric thin films, J. Appl. Phys. **100**, 051607 (2006).

[53] A. K. Tagantsev, E. Courtens, and L. Arzel, Prediction of a low-temperature ferroelectric instability in antiphase domain boundaries of strontium titanate, Phys. Rev. B **64**, 224107 (2001).

[54] E. A. Eliseev, S. V. Kalinin, Y. Gu, M. D. Glinchuk, V. Khist, A. Borisevich, V. Gopalan, L.-Q. Chen, and A. N. Morozovska, Universal emergence of spatially modulated structures induced by flexoantiferrodistortive coupling in multiferroics, Phys. Rev. B **88**, 224105 (2013).

[55] E. A. Eliseev, I. S. Vorotiahin, Y. M. Fomichov, M. D. Glinchuk, S. V. Kalinin, Y. A. Genenko, and A. N. Morozovska, Defect driven flexochemical coupling in thin ferroelectric films, Phys. Rev. B **97**, 024102 (2018).

[56] A. S. Yurkov, Elastic boundary conditions in the presence of the flexoelectric effect, JETP Lett. **94**, 455 (2011).

[57] See *Flexoelectricity in Solids: From Theory to Applications*, edited byA. K. Tagantsev and P. V. Yudin (World Scientific, Singapore, 2016), and references therein.

[58] P. V. Yudin, R. Ahluwalia, and A. K. Tagantsev, Upper bounds for flexocoupling coefficients in ferroelectrics, Appl. Phys. Lett. **104**, 082913 (2014).

[59] I. Dzyaloshinsky, A thermodynamic theory of "weak" ferromagnetism of antiferromagnetics, J. Phys. Chem. Solids **4**, 241 (1958).

[60] Note that if the value of the flexoelectric coupling overcomes the critical value it can change the sign of the "effective" gradient coefficients from positive to negative, which also corresponds to the SMP appearance; see, e.g., A. N. Morozovska, E. A. Eliseev, C. M. Scherbakov, and Y. M. Vysochanskii, Influence of elastic strain gradient on the upper limit of flexocoupling strength, spatially modulated phases, and soft phonon dispersion in ferroics, Phys. Rev. B **94**, 174112 (2016).

[61] J. Bardeen, Surface states and rectification at a metal semiconductor contact, Phys. Rev. **71**, 717 (1947).

[62] M. J. Highland, T. T. Fister, D. D. Fong, P. H. Fuoss, C. Thompson, J. A. Eastman, S. K. Streiffer, and G. B. Stephenson, Equilibrium Polarization of Ultrathin $PbTiO_3$ with Surface Compensation Controlled by Oxygen Partial Pressure, Phys. Rev. Lett. **107**, 187602 (2011).

[63] G. B. Stephenson and M. J. Highland, Equilibrium and stability of polarization in ultrathin ferroelectric films with ionic surface compensation, Phys. Rev. B **84**, 064107 (2011).

[64] S. V. Kalinin, Y. Kim, D. Fong, and A. Morozovska, Surface-screening mechanisms in ferroelectric thin films and their effect on polarization dynamics and domain structures, Rep. Prog. Phys. **81**, 036502 (2018).

[65] A. N. Morozovska, E. A. Eliseev, I. S. Vorotiahin, M. V. Silibin, S. V. Kalinin, and N. V. Morozovsky, Control of polarization hysteresis temperature behavior by surface screening in thin ferroelectric films, Acta Mater. **160**, 57 (2018).

[66] J. X. Zhang, Y. L. Li, Y. Wang, Z. K. Liu, L. Q. Chen, Y. H. Chu, F. Zavaliche, and R. Ramesh, Effect of substrate-induced strains on the spontaneous polarization of epitaxial $BiFeO_3$ thin films, J. Appl. Phys. **101**, 114105 (2007).

[67] E. A. Eliseev, A. N. Morozovska, S. V. Kalinin, Y. L. Li, J. Shen, M. D. Glinchuk, L. Q. Chen, and V. Gopalan, Surface effect on domain wall width in ferroelectrics, J. Appl. Phys. **106**, 084102 (2009).

[68] http://energy.gov/downloads/doe-public-access-plan.